Electronic Supplementary Information

Solid-state lithium metal battery with extended cycling and rate performance by a low-melting alloy interface

Tingting Luo[a], Ling Wang[a], Lei Dai[a], Jiayan Luo[b], Shan Liu*[a]

[a]School of Chemical Engineering, North China University of Science and Technology, Tangshan, 063009, China. E-mail: sliu@ncst.edu.cn
[b]Shanghai Key Laboratory of Advanced High-Temperature Materials and Precision Forming, School of Materials Science and Engineering, Shanghai Jiao Tong University, Shanghai, 200240, China

*Corresponding author.
sliu@ncst.edu.cn

Preparation of solid electrolytes: The solid electrolyte $Li_{1.3}Al_{0.3}Ti_{1.7}(PO_4)_3$ was synthesized by the high-temperature solid-state phase method. Li_2CO_3(99.8%), TiO_2(99.9%) and Al_2O_3(99.5%) were selected as the starting powder and dried in the oven for 24h to remove the moisture in the raw materials. The drying raw materials and $NH_4H_2PO_4$(99%) were weighed according to the stoichiometric ratio, and then performed the first ball milling. After drying, the mixture was ground and calcined at 850 °C for 6h, followed by a second ball mill and high-temperature calcination. The obtained solid electrolyte powder was pressed into an electrolyte pellet with a diameter of 12mm on a single axis of 10 mPa. The electrolytes were sintered for 4h at 800 °C in air and sintered in an alumina crucible. Prior to other measurements and tests, the electrolyte pellets were dry-polished with sandpaper to make their surfaces smooth and contamination-free. Finally, $Li_{1.3}Al_{0.3}Ti_{1.7}(PO_4)_3$ electrolyte pellets with a diameter of 11mm and a thickness of 1mm were obtained.

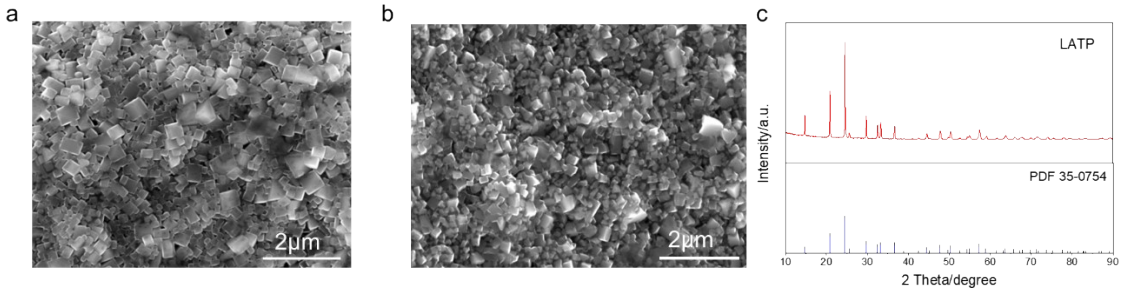

Fig. S1. Surface and cross-sectional SEM images of $Li_{1.3}Al_{0.3}Ti_{1.7}(PO_4)_3$ pellet. (a, b) and XRD pattern of as-prepared LATP and standard $Li_{1.3}Al_{0.3}Ti_{1.7}(PO_4)_3$ (c).

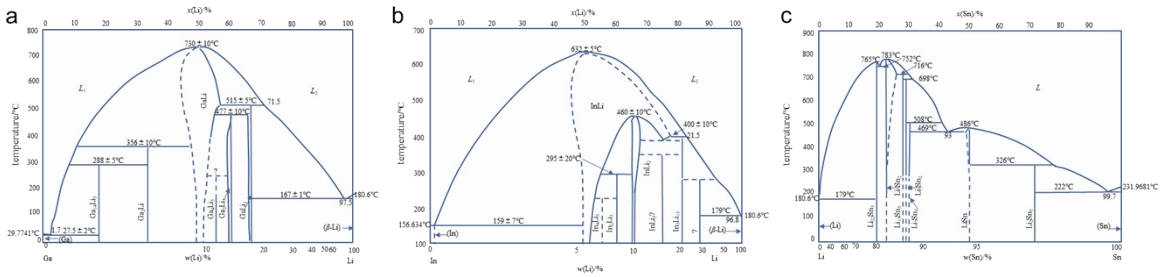

Fig. S2. Phase diagram of the Li-Ga, Li-In and Li-Sn alloy.

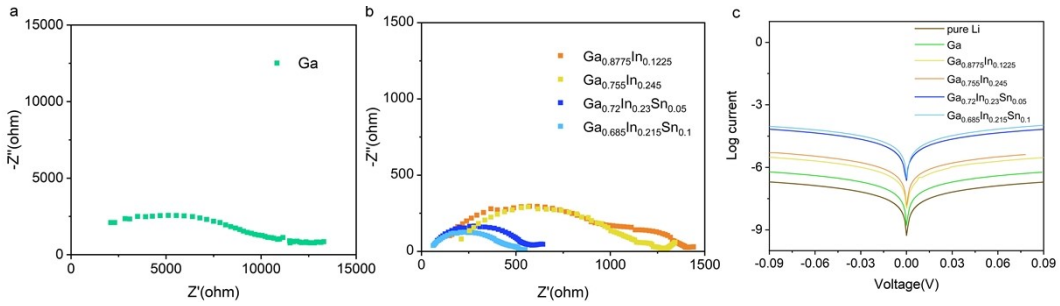

Fig. S3. EIS and Tafel plot of the cell with different elemental contents of the low-melting alloy.

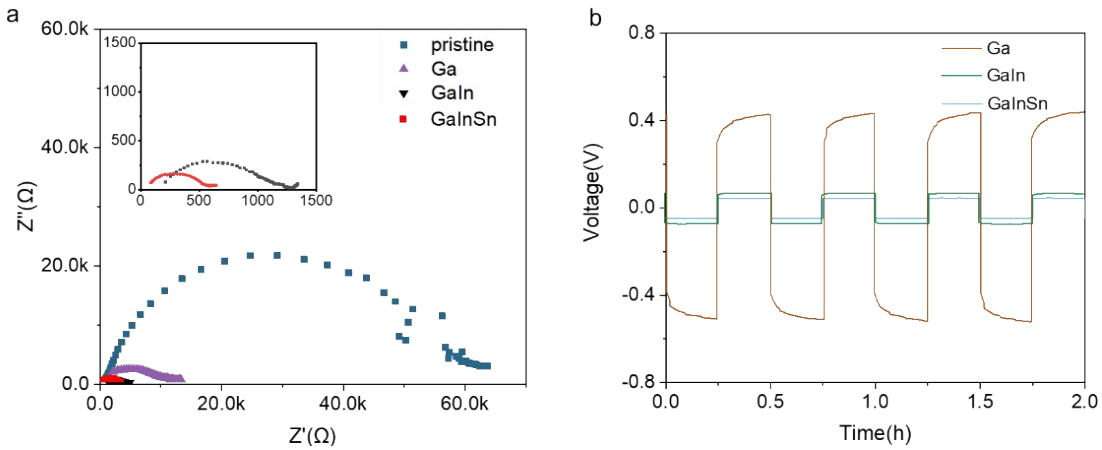

Fig. S4. Interfacial resistance of different liquid metal interlayer (a), the corresponding circular graph at 0.05 mA cm^{-2} (b).

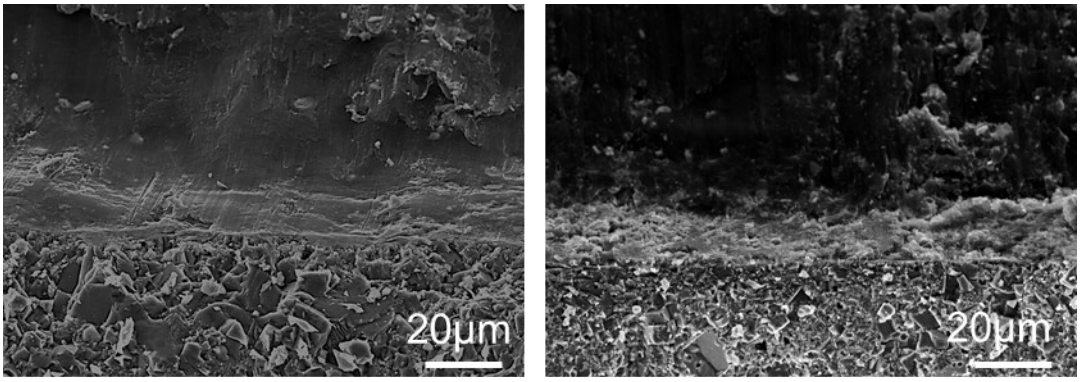

Fig. S5. Cross-section SEM images of before cycling (left) and after cycling (right).

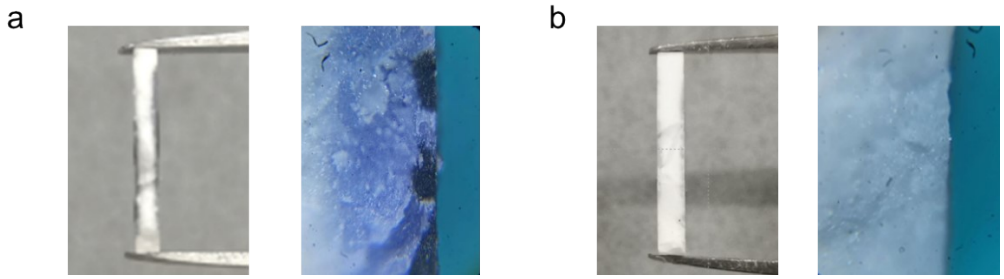

Fig. S6. Cross-sectional optical microscope image of the LATP with pure Li (a), with LMA@Li (b).

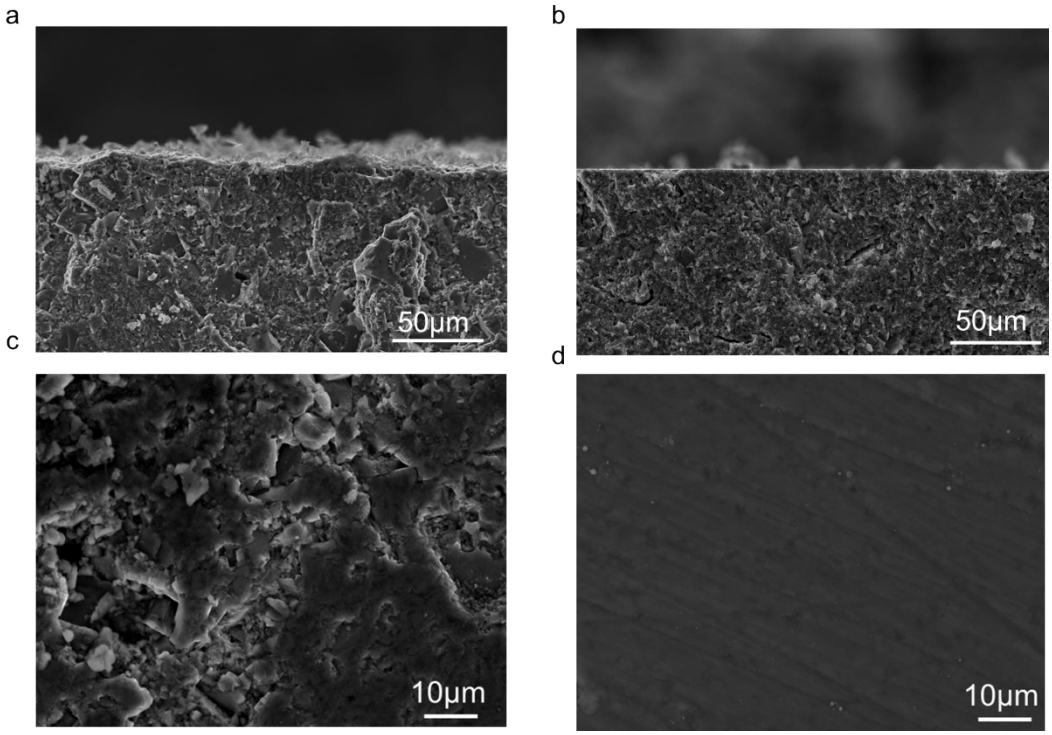

Fig. S7. Cross-sectional SEM image of the cycled LATP with pure Li (a), with LMA@Li (b). Top view SEM image of the LATP with pure Li (c), with LMA@Li (d)

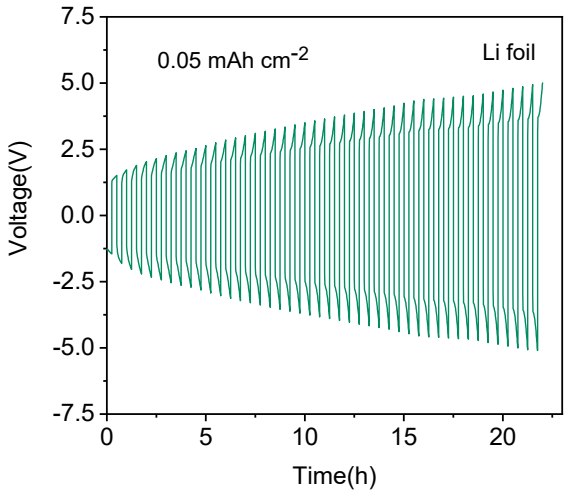

Fig. S8. The Galvanostatic cycling of symmetric cells with pure Li at 0.05 mA cm^{-2}.

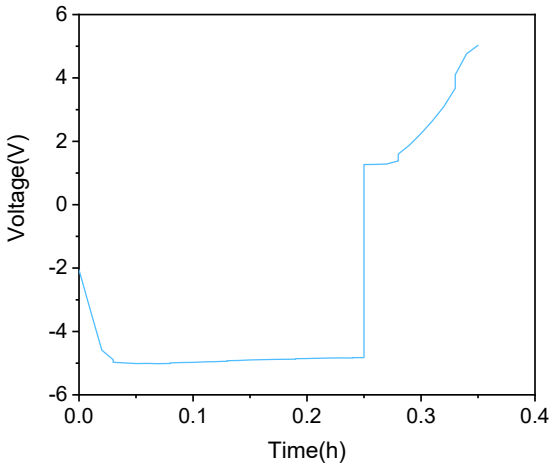

Fig. S9. The Galvanostatic cycling of symmetric cells with pure Li at 0.2 mA cm^{-2}.

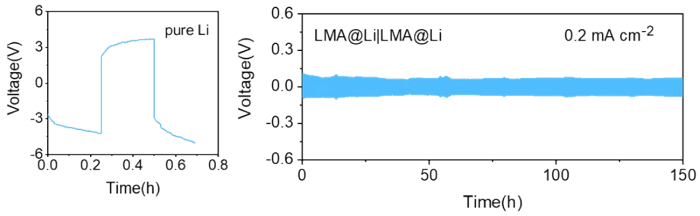

Fig. S10. The voltage profile of pure Li and LMA@Li at 60 oC with 0.2 mA cm-2.

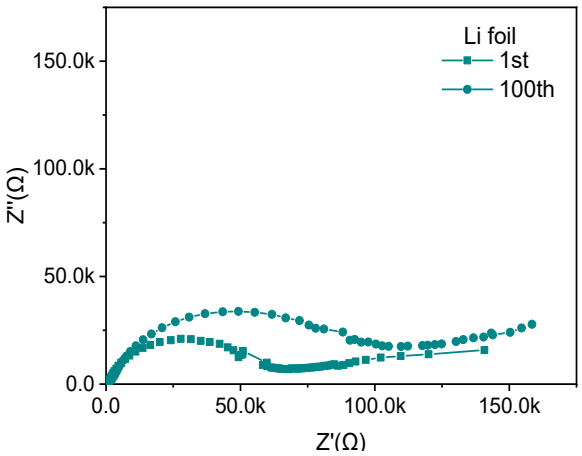

Fig S11. EIS of the symmetric cell with pure Li before cycling and after 100 cycles.

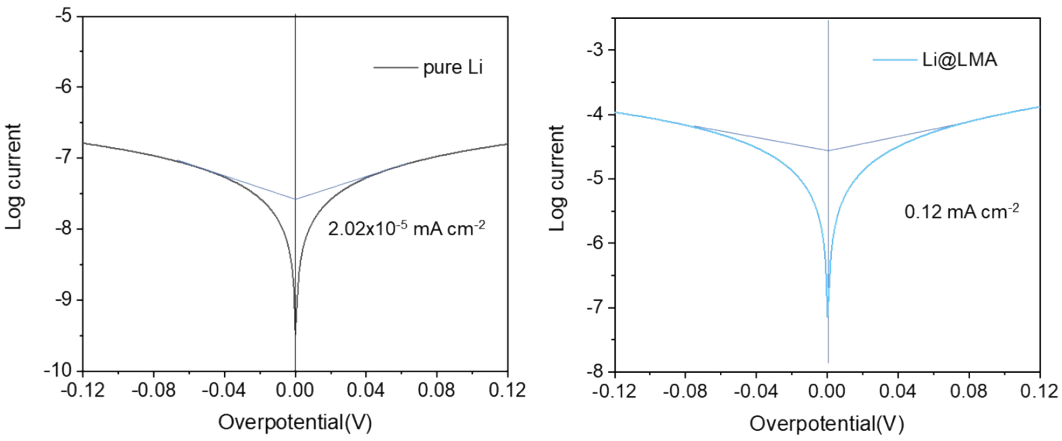

Fig. S12. Tafel plot of LATP with pure Li and LMA@Li.

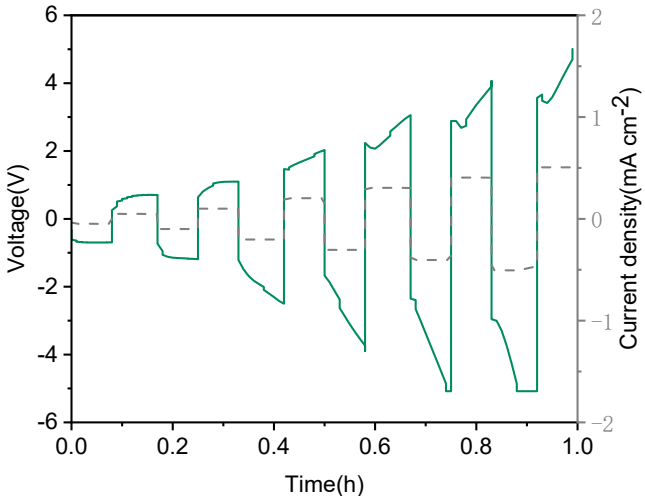

Fig. S13. Rate performance of symmetric cells with pure Li at different current densities from 0.05 to 0.5 mA cm^{-2}

Sample	Crystal structure	a (Å)	b (Å)	c (Å)
$LiTi_2(PO_4)_3$	R-3c	8.513	8.513	20.878
$Li_{1.3}Al_{0.3}Ti_{1.7}(PO_4)_3$	R-3c	8.500	8.500	20.808
Agreement factors: R_p=9.1, R_{wp}=12.8				

Table S1: Results of the refinements of the structural parameters for LATP.

	Binding energy (eV)	FWHM (eV)	Area (%)
Ti^{4+} $2p_{3/2}$	459.9	1.098	36.57
Ti^{3+} $2p_{3/2}$	458.5	1.87	36.48
Ti^{4+} $2p_{1/2}$	465.8	1.37	10.76
Ti^{3+} $2p_{1/2}$	464.4	2.06	17.18

Table S2: Parameters used to curve fit Ti 2p from LATP with pure Li.

	Binding energy (eV)	FWHM (eV)	Area (%)
Ti^{4+} $2p_{3/2}$	459.6	1.53	66.17
Ti^{4+} $2p_{1/2}$	465.3	2.24	33.8

Table S3: Parameters used to curve fit Ti 2p from LATP with LMA@Li.

Table S4. Comparison of cell cycle time of solid lithium metal batteries based on solid-state electrolytes.

Type	Current density (mA cm^{-2})	Overpotential (mV)	Cycle time (h)	Ref.
Si/LLZO/Si	0.1	100	12	[1]
Al_2O_3/LATP/ Al_2O_3	0.01	900	600	[2]
LATP-PEO	0.1	200	200	[3]
Al_2O_3-doped ZnO-LATP	0.1	400	800	[4]
IL@SPF-LATP	0.05	200	850	[5]
Al/LLZO/Al	0.1	25	34	[6]
LMA@Li/LATP/LMA@Li	0.05	50	1200	This work

[1]. W. Luo, Y. Gong, Y. Zhu, K. K. Fu, J. Dai, S. D. Lacey, C. Wang, B. Liu, X. Han, Y. Mo, E. D. Wachsman and L. Hu, Transition from Superlithiophobicity to Superlithiophilicity of Garnet Solid-State Electrolyte. *J. Am. Chem. Soc.*, 2016, 138, 12258-12262.

[2]. Y. Liu, Q. Sun, Y. Zhao, B. Wang, P. Kaghazchi, K. R. Adair, R. Li, C. Zhang, J. Liu, L.-Y. Kuo, Y. Hu, T.-K. Sham, L. Zhang, R. Yang, S. Lu, X. Song and X. Sun, Stabilizing the Interface of NASICON Solid Electrolyte against Li Metal with Atomic Layer Deposition. *ACS Appl. Mater. Interfaces.*, 2018, **10**, 31240-31248.

[3]. Z. Yang, H. Yuan, C. Zhou, Y. Wu, W. Tang, S. Sang and H. Liu, Facile interfacial adhesion enabled LATP-based solid-state lithium metal battery. *Chem. Eng. J.,* 2020, 392, 123650

[4]. H. Bai, J. Hu, Y. Duan, T. Kozawa, M. Naito, J. Zhang and S. Dong, Surface modification of $Li_{1.3}Al_{0.3}Ti_{1.7}(PO_4)_3$ ceramic electrolyte by Al_2O_3-doped ZnO coating to enable dendrites-free all-solid-state lithium-metal batteries. *Ceram. Int*., 2019, **45**, 14663-14668.

[5]. M. Lei, S. Fan, Y. Yu, J. Hu, K. Chen, Y. Gu, C. Wu, Y. Zhang and C. Li, NASICON-based solid state Li-Fe-F conversion batteries enabled by multi-interface-compatible sericin protein buffer layer. *Energy Storage Mater.,* 2022, **47**, 551-560.

[6]. K. Fu, Y. Gong, B. Liu, Y. Zhu, S. Xu, Y. Yao, W. Luo, C. Wang, S. D. Lacey and J. J. S. A. Dai, Toward garnet electrolyte–based Li metal batteries: An ultrathin, highly effective, artificial solid-state electrolyte/metallic Li interface. *Sci. Adv.,* 2017, **3**, e1601659.